CrossMark

Large Angular-scale Multipoles at Redshift ~ 0.8

Prabhakar Tiwari[1] and Pavan K. Aluri[2]
[1] National Astronomical Observatories, CAS, Beijing 100012, People's Republic of China; ptiwari@nao.cas.cn
[2] Department of Physics, Indian Institute of Technology (BHU), Varanasi 221005, India; pavanaluri.phy@itbhu.ac.in

Abstract

We prepare the full sky radio galaxy map ($|b| > 10°$), using the north NRAO VLA Sky Survey and south Sydney University Molonglo Sky Survey galaxy catalogs, and study the large-scale multipole anomalies. These galaxies are roughly at redshift $z \sim 0.8$ and are therefore tracing the matter distribution at very large scales. The quadruple and octopole from the radio galaxy catalog are consistent with ΛCDM for a reasonable value of galaxy bias and we do not find dipole–quadruple–octopole alignment as seen in cosmic microwave background (CMB) temperature maps. The quadrupole direction is roughly 46° away from dipole, and the octopole direction is approximately 33° from dipole. The angle between quadrupole and octopole is around 70°. We have large errors in multipole directions due to shot noise. However, with the data that is currently available we do not find any significant alignment between the $l = 1, 2, 3$ modes. The magnitude of all multipoles, except dipole, are roughly consistent with ΛCDM for reasonable galaxy bias. The dipole magnitude remains inconsistent with CMB as reported in previous studies. Our findings may impose stringent constraints on cosmological models with large-scale anisotropy features.

Key words: dark matter – galaxies: active – galaxies: high-redshift – large-scale structure of universe

1. Introduction

In modern cosmology we assume our universe on a large scale to be statistically homogeneous and isotropic (Milne 1933, 1935). The cosmic microwave background (CMB) is uniform to roughly 1 part in 10^5 (Penzias & Wilson 1965; White et al. 1994; Bennett et al. 2013; Planck Collaboration et al. 2016) and this strongly supports the isotropy assumption. Furthermore, there are other observations of isotropy, such as, for example, ultra-high energy cosmic-ray events from the Telescope Array are isotropic on the sky (Abu-Zayyad et al. 2012), the *Fermi* Gamma-Ray Burst data is isotopic (Řípa & Shafieloo 2017, 2019) and the radio polarization angles from active galactic nuclei are also isotropic (Tiwari & Jain 2019). However, there remain several observations along with signals from CMB itself that suggest a violation of statistical isotropy. In particular the CMB dipole, quadrupole, and octopole modes are roughly aligned and are puzzling within the standard model of cosmology (de Oliveira-Costa et al. 2004a; Ralston & Jain 2004; Schwarz et al. 2004). In the CMB map from nine years of *Wilkinson Microwave Anisotropy Probe* observations, quadrupole and octopole are aligned within 3° (degree) (Bennett et al. 2013). Planck observations also confirm this result where quadrupole and octopole are found to be aligned at 8° to 13° in the foreground cleaned CMB maps produced by the Planck team using various cleaning procedures. The probability of such an alignment to occur is ∼1% to 2.6% (Planck Collaboration et al. 2014) and thus brings into question our assumption of isotropy at large scales of the universe.

The dipole–quadrupole–octopole alignment signal from CMB is unique as we have never been able to have an alternate measure of this signal from some complimentary cosmological observation. CMB anisotropies trace the density perturbations in the universe at redshift ∼1100, when neutral Hydrogen was formed. The density perturbations grew giving rise to galaxies, galaxy clusters, and all the visible/nonvisible

cosmological structure around us. The high density sites of dark matter, the halos, mediated the baryonic matter to form galaxies, and so the galaxy distribution in space is tracing the background dark matter with galaxy bias (Kaiser 1984). Therefore with the large-scale galaxy surveys, we can probe the background dark matter distribution and can test for any large-scale anomalies in it. Any alignment thus observed in large-scale multipoles of the galaxy distribution map will constitute an independent measure of a similar feature in background dark matter distribution that is so far seen (only) in CMB. The galaxies in this work are sitting at redshift around ∼0.8 (Condon et al. 1998; Wilman et al. 2008) and so we will be probing the anomalies, if any, in the background dark matter distribution at this redshift. Nevertheless, it is worth looking at how the observed CMB anomalies (at redshift ∼1100) got transformed with structure formation and how these alignments look in galaxy surveys, if the anomalies are truly cosmological.

The NRAO VLA Sky Survey (NVSS) radio galaxy clustering results, for higher order multipoles ($l > 4$) show an excellent consistency with the standard ΛCDM power spectrum for a reasonable choice of bias parameter (Blake & Wall 2002b; Nusser & Tiwari 2015). However the dipole signal from NVSS galaxies is significantly higher, roughly three times larger than CMB predicted value[3] (Singal 2011; Gibelyou & Huterer 2012; Rubart & Schwarz 2013; Tiwari & Jain 2015; Tiwari et al. 2015; Tiwari & Nusser 2016).

In this work we aim to study the dipole, quadrupole, and octopole modes, and their alignments from radio galaxy catalogs. NVSS covers the sky north of decl. $-40°$ (J2000), which is almost 80% of the celestial sphere; however, the

---

[3] Our local motion with respect to CMB frame is observed as dipole signal in CMB temperature map, which is of the order of few millikelvin (Conklin 1969; Henry 1971; Corey & Wilkinson 1976; Smoot et al. 1977; Kogut et al. 1993; Hinshaw et al. 2009) and corresponds to a speed of 369 ± 0.9 km s^{-1} in the direction $l = 263°99 \pm 0°14$, $b = 48.26 \pm 0°03$ in galactic coordinates (Kogut et al. 1993; Hinshaw et al. 2009). Therefore we also expect a dipole signal in galaxy distribution due to Doppler and aberration effects (Ellis & Baldwin 1984) caused by our local motion.

remaining 20% of the southern sky remains as an obstacle to achieve a confident measure of large-scale multipoles, i.e., quadrupole and octopole. Thankfully, we have the Sydney University Molonglo Sky Survey (SUMSS) in the southern sky and by merging NVSS and SUMSS we achieve a full sky radio galaxy map for latitudes $|b| > 10°$ (Colin et al. 2017). We carefully prepare the NVSUMSS near full sky galaxy catalog and estimate all the multipoles in the number density map. Our NVSUMSS merging method and final catalog differs from Colin et al. (2017). Assuming the bias value determined in Nusser & Tiwari (2015) we compare the estimated multipoles with ΛCDM. Next, we employ the Power tensor method (Ralston & Jain 2004; Samal et al. 2008) to determine the direction of large-scale multipoles and study their alignments.

The outline of the paper is as following. We discuss the data and full sky catalog preparation in Section 2. In Section 3, we review the angular power spectrum, C_l, formulation and discuss its estimation from the data with partial sky coverage ($|b| > 10°$). The clustering results recovered with NVSUMSS are presented in Section 4. A comparison of angular clustering results obtained using two different methods, and their matching and calibration with previous studies is also presented in this section. The dipole–quadrupole–octopole alignment analysis and results are presented in Section 5. We conclude with a discussion of our results in Section 6.

2. Full Sky Radio Galaxy Catalog

2.1. NVSS

The NVSS[4] catalog covers the sky north of decl. $-40°$ (J2000) in equatorial coordinates. This is almost 80% (69% if we mask $|b| < 10°$) of the celestial sphere. The full catalog contains ∼1.7 million sources with integrated flux density[5] $S > 2.5$ mJy at 1.4 GHz and it is complete above 3.5 mJy (Condon et al. 1998). The full width at half maximum resolution of the survey, i.e., FWHM is $45''$ (arcsec) and observations are at nearly uniform sensitivity. The catalog is known to have some systematics, namely, the Galactic contamination, 22 bright extended source locations and significant systematic gradients in surface density for sources fainter than 10 mJy due to array D and DnC configuration (Blake & Wall 2002a). After masking 22 bright extended source sites and Galactic sources with latitudes $|b| < 5°$ the galaxy spatial distribution is reasonably smooth with flux density cut $S = 10$ mJy and above (Blake & Wall 2002b; Nusser & Tiwari 2015).

2.2. SUMSS

The SUMSS[6] catalog covers the sky south of decl. $-30°$ (J2000). The survey is carried out with the Molonglo Observatory Synthesis Telescope operating at 843 MHz (Mauch et al. 2003). The catalog is limited to Galactic latitudes $|b| > 10°$. The catalog is complete above 8 mJy at decl. $\leqslant -50$ and for decl. between -50 and -30 it is complete above 18 mJy at 843 MHz. The survey is uniform over the observation region and with similar FWHM resolution and sensitivity to NVSS.
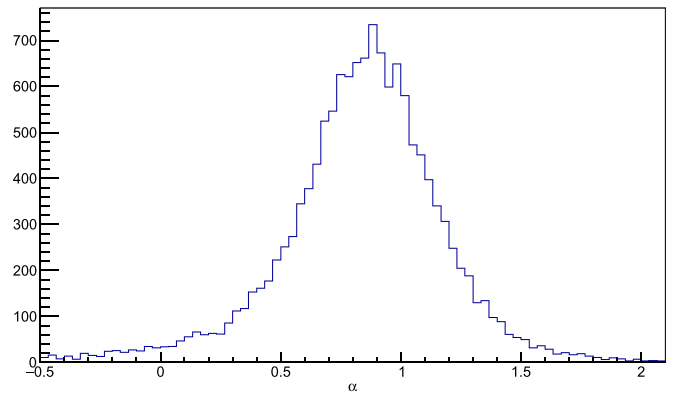
Figure 1. Spectral index with sources common to NVSS and SUMSS. There are 13,942 common sources and following Equation (2) we find a (mean) spectral index of $\alpha = 0.83 \pm 0.35$.

2.3. NVSUMSS

The NVSS and SUMSS operate at different frequencies and thus for a given source the radio flux measurements are different. Nevertheless the radio fluxes at these two frequencies can be linked using the relation,

$$S \propto \nu^{-\alpha}, \tag{1}$$

where α is the spectral index. Therefore for a given source,

$$S_{1.4 \text{ GHz}} = S_{843 \text{ MHz}}(843/1400)^{\alpha}. \tag{2}$$

The two surveys, NVSS and SUMSS, have an overlap region between sky south of decl. $-40°$ to $-30°$. We employ this common survey region to obtain the spectral index α. Considering NVSS and SUMSS position uncertainties we cross-match these catalogs as described below.

We have in total 35,579 sources in SUMSS above 18 mJy in the overlap region of the two surveys. We do find at least one source position match from NVSS for most of the SUMSS sources (35,502 sources out of 35,579) if we consider $45''$ (arcsec) error in R.A. and decl. for all SUMSS's source positions, i.e., looking for an NVSS source within a circle of $45''$ radius around each SUMSS's source. However if we use the source position uncertainties in R.A. and decl. as provided in the catalog, we only match a total of 13,942 positions. The spectral index distribution obtained using the common sources (13,942) between these catalogs following Equation (2) is shown in Figure 1. We find $\alpha = 0.83 \pm 0.35$.

Alternately we can also obtain an estimate of the spectral index as follows. In the common observing region of the two surveys, SUMSS is complete above 18 mJy at 843 MHz and NVSS is complete above 3.5 mJy at 1.4 GHz (note that 18 mJy at 843 MHz corresponds to 12 mJy at 1.4 GHz following Equation (2)). So for a given flux cut which is above the flux completeness limit of both surveys, we expect to see same radio galaxies and thus the number density should match. Indeed, we recover the same number density ($\pm 0.3\%$) from these surveys with $\alpha \approx 0.81$. This value of α is slightly less than the mean spectral index from Figure 1. This tiny deviation may occur as these surveys are at low resolution and dominated by unresolved sources. Furthermore, as the NVSS and SUMSS are operated at different frequencies, the source morphology can affect the observed flux densities. For example, the cores typically have flatter spectra than lobes and thus are relatively bright at a higher frequency survey. This may lead to a slight variation in the source population, e.g., the percentage of FRI
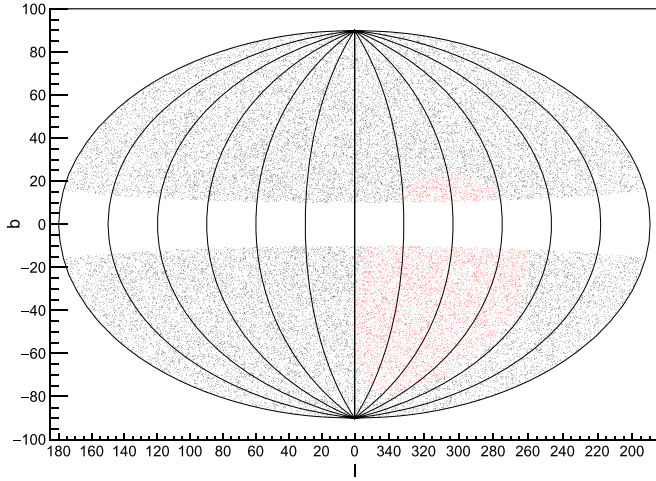
Figure 2. NVSUMSS source distribution with flux cutoff of $S > 15$ mJy at 1.4 GHz. These include SUMSS sources whose flux density is scaled with $\alpha = 0.81$. The NVSS (black) covers the sky north of decl. $-40°$ (J2000) in equatorial coordinates and SUMSS (red) fills the remaining sky. The Aitoff projection shown here is in the galactic coordinates.

and FRII types in these surveys and thus the flux scaling with a power law is not absolutely exact. However, as the survey frequencies are not that far apart and as both surveys have rather low resolution, this is unlikely to be a significant effect.

In our present work we use $\alpha = 0.81$ to scale the SUMSS observed source fluxes from 843 MHz to 1.4 GHz, following Equation (2), and combine them with NVSS sources. We remove Galactic plane $|b| < 10°$ and also 22 bright extended sources and produce our otherwise full sky radio galaxy map, the "NVSUMSS." It spans about 82.74% of the sky and contains 410,308 sources above 15 mJy at 1.4 GHz. The NVSUMSS is complete above 12 mJy at 1.4 GHz (since 12 mJy at 1.4 GHz corresponds to 18 mJy at 843 MHz—the SUMSS completeness limit). NVSUMSS catalog in Aitoff projection in the galactic coordinates is shown in Figure 2.
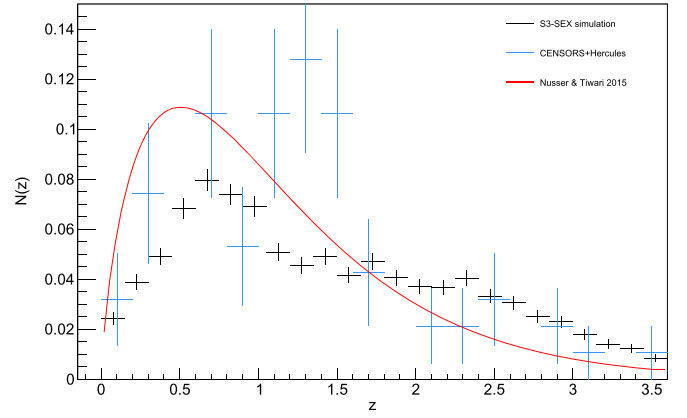
2.4. The Redshift Distribution

The redshift information for the NVSS and SUMSS sources is unavailable. However, we can reasonably model the redshift distribution for our NVSUMSS catalog following semi-empirical simulation provided by Wilman et al. (2008). Alternatively we can follow Nusser & Tiwari (2015) and model the redshift distribution by relying on CENSORS (Best et al. 2003; Rigby et al. 2011) and Hercules (Waddington et al. 2000, 2001) surveys of radio galaxies where the redshifts are available. The CENSORS survey contains 135 radio sources, selected from the NVSS, over 6 deg^2 of the sky and complete down to 7.2 mJy at 1.4 GHz. On the other hand, the Hercules survey contains 64 objects over 1.2 deg^2 and complete above 2 mJy at 1.4 GHz. The two surveys together contain 94 sources for $S > 15$ mJy. We have plotted the redshift distribution following Wilman et al. (2008) simulation and CENSORS +Hercules catalogs in Figure 3. We notice that the redshift distribution peaks roughly at $z \sim 0.8$.

3. The Galaxy Clustering Angular Power Spectrum

3.1. Theoretical C_l

Here we briefly review the relationship between the galaxies' spatial distribution and background dark matter following the

Figure 3. Redshift distribution models. The S^3-SEX is an extragalactic radio continuum simulation by Wilman et al. (2008). We have also plotted the redshift distribution from CENSORS+Hercules catalogs and a fit to this as given in Nusser & Tiwari (2015). Both histograms are for $S > 15$ mJy at 1.4 GHz, the horizontal error bars are bin size and the vertical error bars are the square root of the corresponding bin count.

ΛCDM scenario. Let $\mathcal{N}(\hat{\boldsymbol{r}})$ be the projected number density per steredian in the direction $\hat{\boldsymbol{r}}$. We can write this as,

$$\mathcal{N}(\hat{\boldsymbol{r}}) = \bar{\mathcal{N}}(1 + \Delta(\hat{\boldsymbol{r}})), \tag{3}$$

where $\bar{\mathcal{N}}$ is the mean number density, and $\Delta(\hat{\boldsymbol{r}})$ represents the projected number density contrast. $\Delta(\hat{\boldsymbol{r}})$ is theoretically connected to the background dark matter density contrast, $\delta_m(\boldsymbol{r}, z(r))$. Here $\boldsymbol{r}$ stands for comoving distance r in direction $\hat{\boldsymbol{r}}$ and $z(r)$ is the redshift corresponding to comoving distance r. Assuming linear galaxy biasing $b(z)$, we can write the galaxy density contrast as

$$\delta_g(\boldsymbol{r}, z(r)) = \delta_m(\boldsymbol{r}, z = 0)D(z)b(z), \tag{4}$$

where $D(z)$ is the linear growth factor and $z = z(r)$. Following these we get,

$$\Delta(\hat{\boldsymbol{r}}) = \int_0^\infty \delta_g(\boldsymbol{r}, z(r))p(r)dr$$
$$= \int_0^\infty \delta_m(\boldsymbol{r}, z = 0)D(z)b(z)p(r)dr, \tag{5}$$

where $p(r)dr$ is the probability of observing galaxy between comoving distance r and $(r + dr)$. Note that $\Delta(\hat{\boldsymbol{r}})$ may have some additional contributions from redshift distortions, physical distance fluctuations, and variation of radio source luminosities and spectral indices (Chen & Schwarz 2015). However, these effects are expected to be tiny and we can safely ignore them in this work. We next expand $\Delta(\hat{\boldsymbol{r}})$ in spherical harmonics as,

$$\Delta(\hat{\boldsymbol{r}}) = \sum_{lm} a_{lm} Y_{lm}(\hat{\boldsymbol{r}}). \tag{6}$$

We invert the above equation to recover a_{lm} as,

$$a_{lm} = \int d\Omega \Delta(\hat{\boldsymbol{r}}) Y_{lm}^*(\hat{\boldsymbol{r}})$$
$$= \int d\Omega Y_{lm}^*(\hat{\boldsymbol{r}}) \int_0^\infty \delta_m(\boldsymbol{r}, z = 0)D(z)b(z)p(r)dr. \tag{7}$$

The dark matter density field $\delta_m(\boldsymbol{r}, z = 0)$ can be written as a Fourier transform of k-space density field δ_k, as

$$\delta_m(\boldsymbol{r}, z = 0) = \frac{1}{(2\pi)^3} \int d^3 k \delta_k e^{i\boldsymbol{k} \cdot \boldsymbol{r}}. \qquad (8)$$

Here we can substitute,

$$e^{i\boldsymbol{k} \cdot \boldsymbol{r}} = 4\pi \sum_{l,m} i^l j_l(kr) Y_{lm}^*(\hat{\boldsymbol{r}}) Y_{lm}(\hat{\boldsymbol{k}}), \qquad (9)$$

where j_l is the spherical Bessel function of first kind for integer l. Subsequently we write

$$a_{lm} = \frac{i^l}{2\pi^2} \int dr D(z) b(z) p(r) \int d^3 k \delta_{\boldsymbol{k}} j_l(kr) Y_{lm}^*(\hat{\boldsymbol{k}}). \qquad (10)$$

Now we can obtain an expression for the corresponding angular power spectrum, C_l, as

$$
\begin{aligned}
C_l &= \langle |a_{lm}|^2 \rangle \\
&= \frac{2}{\pi} \int dk k^2 P(k) \left| \int_0^\infty D(z) b(z) p(r) dr j_l(kr) \right|^2 \\
&= \frac{2}{\pi} \int dk k^2 P(k) W^2(k), \qquad (11)
\end{aligned}
$$

where $P(k)$ is ΛCDM power spectrum, and $W(k) = \int_0^\infty D(z) b(z) p(r) dr j_l(kr)$ is the window function in k-space. We have used $\langle \delta_k \delta_{k'} \rangle = (2\pi)^3 \delta^D(\boldsymbol{k} - \boldsymbol{k}') P(k)$ where δ^D is Dirac's δ−function.

3.2. Measured C_l from Galaxy Surveys

The galaxy surveys in reality never cover the full sky and we have some regions with no data or bad data in the sky. Therefore, in general, the measured C_l are always from partial sky. Furthermore, we are limited by galaxy number density and thus we have shot noise in C_l measurements. An estimate of C_l corresponding to the theoretical C_l given in Equation (11) is,

$$C_l^{obs} = \frac{\langle |a'_{lm}|^2 \rangle}{J_{lm}} - \frac{1}{\bar{\mathcal{N}}}, \qquad (12)$$

where $a'_{lm} = \int_{survey} d\Omega \Delta(\hat{\boldsymbol{r}}) Y_{lm}^*(\hat{\boldsymbol{r}})$ and $J_{lm} = \int_{survey} |Y_{lm}|^2 d\Omega$, the J_{lm} is the approximate correction for the partial survey region following Peebles (1980). The term $\frac{1}{\bar{\mathcal{N}}}$ is deducted to remove the contribution from Poissonian shot noise. Note that $\bar{\mathcal{N}}$ is the mean number density. The 1σ error in this estimate due to cosmic variance, sky coverage, and shot noise is,

$$\Delta C_l = \sqrt{\frac{2}{(2l + 1) f_{sky}}} \left(C_l^{obs} + \frac{1}{\bar{\mathcal{N}}} \right), \qquad (13)$$

where f_{sky} is the fraction of the sky observed in the survey.

4. Clustering Power Spectrum from NVSUMSS

We use the HEALPix[7] (Gořski et al. 2005) pixelization scheme to produce equal area pixels on the spherical surface. We next populate the map with our NVSUMSS catalog and this gives the number density map $\mathcal{N}(\hat{\boldsymbol{r}})$, i.e., the number of sources in a pixel in direction $\hat{\boldsymbol{r}}$. We use an $N_{side} = 64$
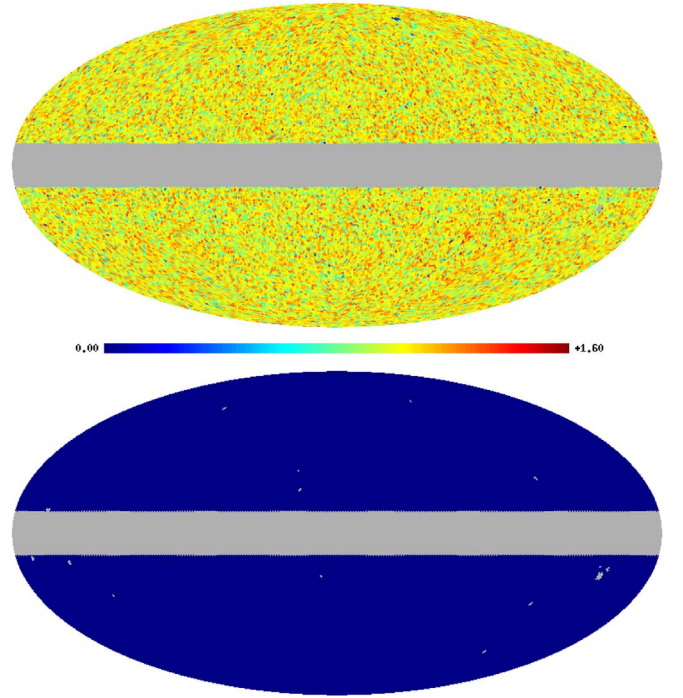
Figure 4. Top: the number density $\log_{10}(1+N)$ map obtained using NVSUMSS with S > 15 mJy at 1.4 GHz. Here N denotes the number of sources in Healpix pixels. We have used $N_{side} = 64$. Bottom: the corresponding source mask that denotes the extent of the sky covered by the composite catalog.

HEALPix grid to generate our number density map. The map thus obtained and the source mask are shown in Figure 4.

We obtain C_l^{obs} and its error bars following Equations (12) and (13), respectively. The NVSS and SUMSS have broad angular resolution and around 90% of sources are unresolved in these surveys. The radio-loud sources often have extended radio emission and the resolved 10% of the population may have multiple entries in the catalog. Blake et al. (2004) noted that this has a small but measurable effect on angular power spectrum as a fixed offset to C_l given by $\Delta C_l \approx 2e/\bar{\mathcal{N}}$, where $e = 0.070 \pm 0.005$. Note the factor $1/\bar{\mathcal{N}}$, which is the shot noise contribution. Thus we also deduct this fixed offset from all C_l in estimating C_l^{obs}.

The C_l^{obs} from NVSUMSS are shown in Figure 5. The NVSUMSS C_l agree with C_l obtained using only NVSS sources by Nusser & Tiwari (2015). The solid curve in Figure 5 denotes the ΛCDM angular power spectrum following the bias, $\boldsymbol{b}(z) = 0.33z^2 + 0.85z + 1.6$, and $N(z) \propto z^{0.74} \exp\left[-\left(\frac{z}{0.71} \right)^{1.1} \right]$ schemes given in Nusser & Tiwari (2015). We conclude that the clustering results from NVSUMSS are similar to NVSS and agrees well with ΛCDM predictions. This confirms that our NVSUMSS catalog is free from systematics and unusual clustering.

Since the main aim of the paper is to study the large angle multipoles, i.e., low-l modes we use the iSAP inpainting package (Abrial et al. 2007, 2008; Fourt et al. 2013) to construct full sky a_{lm} from the partial sky map surface number density contrast map shown in Figure 4. iSAP stands for Interactive Sparse Astronomical Data Analysis Packages.[8] As the name says, it provides various tools for astronomical image
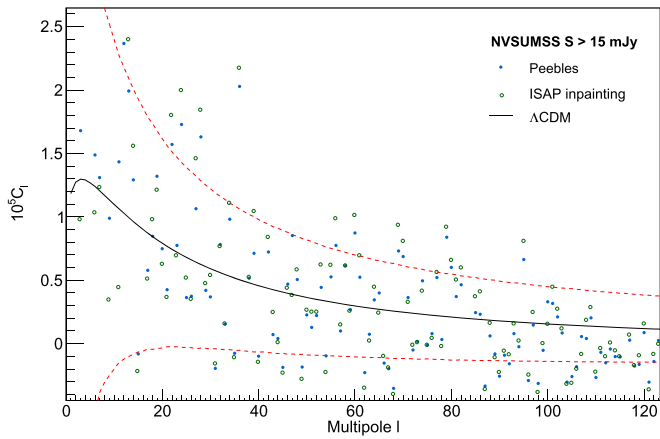
Figure 5. Angular power spectrum estimated from the NVSUMSS catalog with flux density cut S > 15 mJy at 1.4 GHz. The blue filled circles are C_l^{obs} following Equation (12). The solid line is ΛCDM values. The dashed lines are 1σ limits due to shot noise and cosmic variance scatter and f_{sky} (Equation (13)). The open circles are C_l^{obs} recovered using the iSAP inpainting scheme (Fourt et al. 2013; Starck et al. 2013).

Figure 6. NVSUMSS number density contrast map histogram as seen in Healpix pixels. The inpainted full sky distribution is shown in solid black and the input partial sky distribution is shown in blue. The recovered inpainted pixels distribution is shown in red. The input sky distribution and inpainted pixels histograms are scaled by a factor of 49,152/40,667 and 49,152/8485, respectively, for comparison between the histograms.
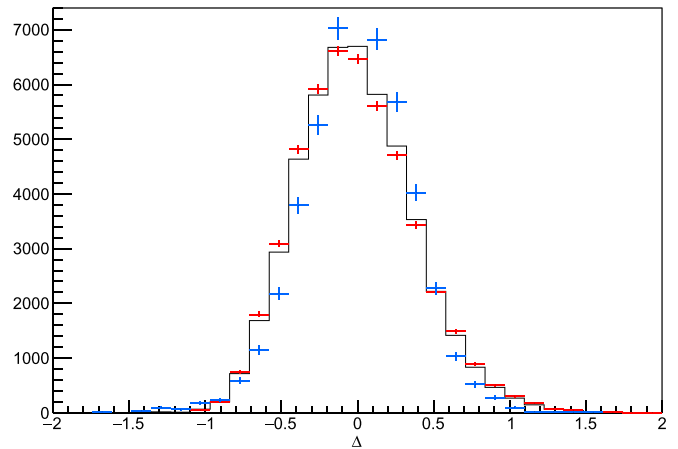
analysis based on Sparsity (Starck et al. 2015). If the absolute sorted data coefficients (in descending order) in a suitable basis decay fast typically as a power law, then the data is said to be Sparse. In the case of a CMB anisotropy field, the sorted absolute values of its spherical harmonic coefficients decay quickly. Furthermore, no assumptions of isotropy or Gaussianity need to be made in restoring the missing regions due to masking, of an otherwise full sky CMB map. However, these tools can also be applied to random fields, which are expected to be isotropic and Gaussian. It was also found through simulation of CMB maps that sparsity based inpainting does not alter the significance of any non-Gaussian or anisotropic feature of our interest already present in a CMB map (Starck et al. 2013), if the masking fraction is less than 20%. The default setting of the iSAP inpainting package were used to inpaint the masked portions of the sky as shown in the bottom panel of Figure 4.

We have shown the inpainted full sky pixel distribution along with input partial map in Figure 6. The power spectrum from the inpainted number density map is also shown in Figure 5 along with the one estimated using the classical method of Peebles (1980). The power spectra recovered from both the methods match reasonably well with each other within the error bars. We note that, at low-l, the error bars in C_ls due to cosmic variance are large.

5. Dipole–quadrupole–octopole Alignment Analysis

5.1. Power Tensor

In order to test for alignments among various multipoles we use the Power tensor method introduced in Ralston & Jain (2004). The method involves associating a preferred axis or axis of anisotropy with each multipole. Then their orientations can be compared by taking a simple inner product of the preferred axis associated with the multipoles in question. For a range of multipoles, one can also compare their alignments using what is called an "Alignment tensor," given by Samal et al. (2008).

Power tensor is defined as a quadratic estimator in terms of spherical harmonic coefficients, a_{lm}, of a multipole "l" as

$$A_{ij}(l) = \sum_{m,m'm''} a_{lm} J^i_{mm'} J^j_{m'm''} a_{lm''} \quad (14)$$

where J_i (i = 1, 2, 3) are the angular momentum matrices in spin−l representation. A normalization factor of $1/(l(l+1)(2l+1))$ is chosen such that the trace of this 3×3 Power tensor matrix corresponding to a multipole, l, is equal to the total power, C_l, of that multipole.

The Power tensor $A_{ij}(l)$ maps a multipole, or analogously a_{lm}s, to an ellipsoid. Let Λ_α and e_α denote the three eigenvalues and eigenvectors of the Power tensor respectively. These eigenvectors form the three perpendicular axes of the ellipsoid and the corresponding (normalized) eigenvalues denote the length of each axis. We associate that eigenvector, which has the largest eigenvalue among the three Λ_α's, as the preferred axis or the axis of anisotropy of a multipole l. Stated differently, the axis along which the ellipsoid is most elongated is taken as the axis of anisotropy of that multipole. We call this axis the principal eigenvector (PEV) of that multipole. In the case of statistical isotropy all the eigenvalues of $A_{ij}(l)$ will be equal to $C_l/3$ and the PEVs will be oriented randomly. For further details about the Power tensor method the reader may refer to Ralston & Jain (2004); Samal et al. (2008).

In order to test or quantify isotropy of CMB maps, many other methods were also used, such as, for example, angular momentum dispersion (AMD) maximization (de Oliveira-Costa et al. 2004b), Maxwell's multipole vectors (MMVs; Schwarz et al. 2004) and bipolar spherical harmonics (BipoSH; Hajian & Souradeep 2003). Given the similarity of our statistic with the AMD statistic, which involves repeated search over the sky for an anisotropy axis that maximizes this statistic, we expect to obtain the same results. MMVs involve factoring the spherical harmonic coefficients of a CMB map corresponding to a multipole "l" to get "l" unit vectors, which can be used to study spurious alignment preferences in a CMB map that breaks isotropy. The BipoSH framework can be used to quantify (an)isotropy of a CMB map using any spurious correlations present between different multipoles induced by an

Table 1
Dipole, Quadrupole, and Octopole Magnitudes and Directions from NVSUMSS with Flux Density Cut of $S > 15$ mJy at 1.4 GHz

l	C_l^{obs} ($\times 10^4$)			Direction (iSAP)	
	ΛCDM	Peebles	iSAP	(l, b)	(R.A., Decl.)
1	0.127	2.141	2.234	253, 19	141, −23
2	0.130	0.776	0.559	306, 5	199, −58
3	0.129	0.168	0.098	266, 46	168, −10

Note. The shot noise, $\frac{1}{N}$, for this flux cut is 2.5×10^{-5}.

underlying anisotropic field and can further be used to reconstruct that anisotropic field itself using those correlations (Aluri et al. 2015), which otherwise will be statistically consistent with zero under the assumption of isotropy. Given the number counts data as is available right now—in terms of noise levels, galactic cuts, etc., in the present work we, however, use only the Power tensor method and report our results and analysis thus obtained.

5.2. Alignment Analysis with the Power Tensor

The amplitude of dipole as observed with NVSS and NVSS +SUMSS remains high and disagrees with CMB kinematic dipole (Singal 2011; Gibelyou & Huterer 2012; Rubart & Schwarz 2013; Tiwari & Jain 2015; Tiwari et al. 2015; Tiwari & Nusser 2016; Colin et al. 2017). The magnitude of quadrupole is roughly 1σ away from ΛCDM prediction and octopole magnitude is almost the same as ΛCDM prediction. The observed power, C_l^{obs}, for $l = 1$, 2, 3, i.e., dipole, quadrupole, and octopole modes are given in Table 1. The preferred direction, i.e., PEV direction inferred for these multipoles using the Power tensor are also listed in the same table. We recall that these multipole directions are derived using spherical harmonic coefficients of the full sky projected number density map obtained using the iSAP inpainting procedure. The multipole power and preferred direction results for $l = 1$, 2, and 3 with different flux density cuts are given in Table 2. We note that the dipole direction and magnitude obtained with NVSUMSS match those of previous studies (Tiwari & Nusser 2016; Colin et al. 2017). The dipole, quadrupole, and octopole directions vary with flux density cuts but roughly remain stable. These multipole directions for various flux density cuts are also shown in Figure 7. We have also shown the CMB's dipole, quadrupole, and octopole directions in the same figure. The quadrupole and octopole directions obtained using the power tensor method are given in Table 3.

The angle between dipole, quadrupole, and octopole for various flux density cuts are given in Table 4. The average angle between dipole and quadrupole is ≈46° and with octopole it is ≈33°. The quadrupole and octopole are ≈70° away from each other on average. If we assume that the quadrupole and octopole directions are random and have no alignment with dipole, then the probabilities of observed alignments are 0.30 and 0.16 for quadrupole–dipole and octopole–dipole, respectively. The probability of having quadrupole and octopole within 70° is 0.66. This is statistically consistent with random orientation of multipole directions as expected in standard cosmology based on Cosmological principle. Note that the multipole directions are axes and their orientation is random over the sky. Therefore the angle

Table 2
Dipole, Quadrupole, and Octopole Directions from NVSUMSS with Flux Density Cut $S > 20, 30, 40,$ and 50 mJy. The Shot Noise, $\frac{1}{N}$, for Corresponding Flux Cuts is Also Given

S	(l, b)			Shot Noise	Total Sources Over
(>mJy)	$l = 1$	$l = 2$	$l = 3$	($\times 10^5$)	$f_{sky} = 0.8274$
20	258, 21	304, −14	235, 42	3.2	321,899
30	264, 22	302, 2	238, 19	4.7	221349
40	267, 6	306, −11	242, 30	6.2	166,770
50	290, 11	300, −19	238, 20	7.8	132,455
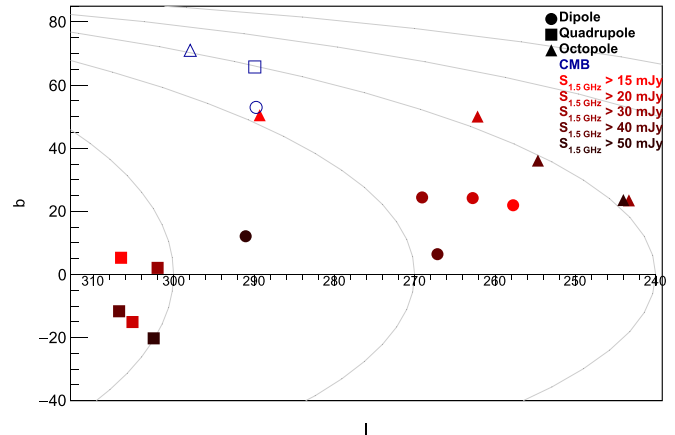
Figure 7. Dipole, quadrupole, and octopole directions from NVSUMSS in galactic coordinates are shown here by filled circle, square, and triangular data points respectively. They are shown in dark to light red in color for flux density cuts of $S > 15, 20, 30, 40,$ and 50 mJy. For comparison, we also show the CMB's quadrupole and octopole directions (in blue) as computed by us using the latest NILC CMB map from PLANCK public release 3, along with the dipole direction. These directions (of $l = 2, 3$) are listed in Table 3.

Table 3
CMB's Quadrupole and Octopole Directions as Found in the Latest NILC and SMICA CMB Maps from PLANCK Public Release 3, Obtained Using the Power Tensor Method

CMB Map	(l, b)	
	$l = 2$	$l = 3$
NILC	241, 58	238, 63
SMICA	240, 54	238, 63

Table 4
Angular Distance between Dipole, Quadrupole, and Octopole Directions from NVSUMSS with Flux Density Cut $S > 15, 20, 30, 40, 50$ mJy

Multipoles	Angle Between (in degrees)					Mean
	$S > 15$	$S > 20$	$S > 30$	$S > 40$	$S > 50$	
$l12$	54	58	42	43	32	46
$l13$	29	28	25	34	50	33
$l23$	54	85	65	76	72	70

Note. The last column is the average (over flux density cuts) angle between multipoles.

between two multipoles can be a maximum of 90° and the probability of having two multipoles aligned within angle α is $\int_0^\alpha \sin(\theta) d\theta$.

Table 5
Expected Uncertainty in Dipole, Quadrupole, and Octopole Directions Due to Shot Noise and Partial to Full Sky Recovery with Flux Density Cut $S > 20, 30, 40, 50$ mJy Δl and Δb are the 1σ Errors (i.e., 68% Confidence Level) in l and b, Respectively

S	$(\Delta l, \Delta b)$		
($>$mJy)	$l = 1$	$l = 2$	$l = 3$
15	16, 12	18, 17	65, 23
20	14, 11	21, 25	63, 23
30	15, 13	19, 21	45, 31
40	14, 14	26, 17	41, 28
50	18, 14	31, 28	40, 27

Note. Note the shot noise for these flux cuts in Table 2.

5.3. Multipole Direction Error Estimate

In Figure 7 we have shown the multipole directions with different flux density cuts. The scatter in multipole directions reflects the effect of shot noise, partial to full sky construction, etc. To determine the effect of masking and shot noise, we resort to mocks and emulate the NVSUMSS multipole recovery as follows. We consider the NVSUMSS density contrast map, $m0$, and the multipole directions from this density contrast map as our model and input directions respectively. The NVSUMSS galaxy number count map, m, with different flux cuts, $S > 15$ to 50 mJy, is simply $m(i) = (m0(i) + 1) \times \bar{p}$, where i stands for pixel and $\bar{p}$ is the mean number of galaxies in pixels, i.e., pixel area $\times$ number density ($\bar{\mathcal{N}}$). We call Poisson distribution at every pixel and prepare a new map, m_{poi}. The pixels in the m_{poi} map are given by, $m_{poi}(i) = $ Poisson $(m(i))$. Note that the map m_{poi} contains both the shot noise (i.e., $1/\bar{\mathcal{N}}$) and the model map m. To emulate the effect of partial to full sky recovery we employ the same NVSUMSS mask and use the iSAP inpainting package to recover a full sky map from partial m_{poi}. We call this new map the m'_{poi} map. Next we construct a density contrast map from m'_{poi} and apply the Power tensor method to obtain multipole directions. The multipoles' magnitude and direction thus recovered, contain the model input map, $m0$, and shot noise, and also include uncertainties due to partial- to full sky construction. We determine the uncertainty in the recovered PEV directions using a large ensemble of Poissonian maps generated as described above. The results are presented in Table 5. We note that the direction recovery for the NVSUMSS octopole for flux cut $S > 15$ and 20 mJy shows a very large error in longitude. The scatter in recovered multipole directions is largely due to shot noise. With mocks we notice that approximately 90% of the dipole directional error is from shot noise and the remaining comes from masking and partial to full sky recovery.

6. Conclusion

The galaxy distribution traces the background dark matter density. The radio galaxy surveys observe the galaxies at relatively large redshift, i.e., $z \sim 1$ over a large fraction of the sky, and therefore galaxies in these surveys are potential tracers of large-scale matter distribution in the universe. In this work we combine the north NVSS and the south SUMSS radio galaxy catalogs and created a composite catalog that traces the large-scale matter distribution. After removing Galactic plane with latitude $\pm 10°$ and other bright locations we get $\sim 83\%$ of

the sky coverage with a number density ~ 12 sources degree^{-2} for flux density cut of $S > 15$ mJy at 1.4 GHz.

The SUMSS is at 843 MHz and NVSS is at 1.4 GHz. Therefore, to combine these surveys, we obtain the spectral index for extrapolation of fluxes in frequency from the overlap region, and scale the SUMSS 843 MHz fluxes appropriately to 1.4 GHz. A spectral index is chosen so as to achieve an accurate number density match between these two surveys above the flux completeness limits. We further calibrate the clustering results from this combined NVSUMSS catalog with previous works (Tiwari & Nusser 2016; Colin et al. 2017) and find a good match. Except for dipole, all other multipoles match with ΛCDM predictions for a reasonable choice of galaxy bias values given in Nusser & Tiwari (2015). The dipole signal remains high and its magnitude and direction matches with previous studies (Tiwari & Nusser 2016; Colin et al. 2017).

We studied the large-scale anomalies, i.e., low-l power spectrum, in detail and found that the quadrupole and octopole modes are nearly consistent with standard ΛCDM. The quadrupole and octopole preferred axes are on average 46° and 33° (degrees) away from dipole respectively. The average separation between quadrupole and octopole is 70°. We also find that there are large uncertainties in the recovered multipole anisotropy axes, primarily due to shot noise. Particularly the octopole direction for different flux cuts is found to be unstable. With the data as is currently available we do not find significant dipole–quadrupole and quadrupole–octopole alignment. However, we see that the angular separation between dipole–octopole is relatively small, and there may be a possible alignment between them. We will have better resolution on these anisotropies and anomalies with upcoming Square Kilometre Array observations (Ghosh et al. 2016). Nevertheless, this work is an independent assessment of large-scale anomalies observed so far only in CMB data. The results of this work support large-scale isotropy, which is one of the fundamental assumptions of modern cosmology, and thus impose stringent constraints on anisotropic cosmological models and on physical mechanisms introduced to break statistical isotropy on large scales (Hu & Sugiyama 1995; Gordon et al. 2005; Ackerman et al. 2007; Emir Gümrükçüoglu et al. 2007; Koivisto & Mota 2008; Ghosh 2014).

We conclude that with the available radio galaxy catalogs at present, the large-scale multipole directions of the matter distribution around us, are random as expected in standard ΛCDM and we do not find CMB like dipole–quadrupole–octopole alignment. The matter distribution at redshift $z \sim 0.8$ is a good match with ΛCDM (except for dipole power).

References

Abrial, P., Moudden, Y., Starck, J.-L., et al. 2007, JFAA, 13, 729
Abrial, P., Moudden, Y., Starck, J.-L., et al. 2008, StMet, 5, 289
Abu-Zayyad, T., Aida, R., Allen, M., et al. 2012, ApJ, 757, 26
Ackerman, L., Carroll, S. M., & Wise, M. B. 2007, PhRvD, 75, 083502
Aluri, P. K., Pant, N., Rotti, A., & Souradeep, T. 2015, PhRvD, 92, 083015
Bennett, C. L., Larson, D., Weiland, J. L., et al. 2013, ApJS, 208, 20

Best, P. N., Arts, J. N., Röttgering, H. J. A., et al. 2003, MNRAS, 346, 627
Blake, C., Ferreira, P. G., & Borrill, J. 2004, MNRAS, 351, 923
Blake, C., & Wall, J. 2002a, Natur, 416, 150
Blake, C., & Wall, J. 2002b, MNRAS, 329, L37
Chen, S., & Schwarz, D. J. 2015, PhRvD, 91, 043507
Colin, J., Mohayaee, R., Rameez, M., & Sarkar, S. 2017, MNRAS, 471, 1045
Condon, J. J., Cotton, W. D., Greisen, E. W., et al. 1998, AJ, 115, 1693
Conklin, E. K. 1969, Natur, 222, 971
Corey, B. E., & Wilkinson, D. T. 1976, BAAS, 8, 351
de Oliveira-Costa, A., Tegmark, M., Zaldarriaga, M., & Hamilton, A. 2004a, PhRvD, 69, 063516
de Oliveira-Costa, A., Tegmark, M., Zaldarriaga, M., & Hamilton, A. 2004b, PhRvD, 69, 063516
Ellis, G. F. R., & Baldwin, J. E. 1984, MNRAS, 206, 377
Emir Gümrükçüoglu, A., Contaldi, C. R., & Peloso, M. 2007, JCAP, 11, 005
Fourt, O., Starck, J.-L., Sureau, F., et al. 2013, iSAP: Interactive Sparse Astronomical Data Analysis Packages, Astrophysics Source Code Library, ascl:1303.029
Ghosh, S. 2014, PhRvD, 89, 063518
Ghosh, S., Jain, P., Kashyap, G., et al. 2016, JApA, 37, 1
Gibelyou, C., & Huterer, D. 2012, MNRAS, 427, 1994
Gordon, C., Hu, W., Huterer, D., & Crawford, T. 2005, PhRvD, 72, 103002
Gofski, K., Hivon, E., Banday, A., et al. 2005, ApJ, 622, 759
Hajian, A., & Souradeep, T. 2003, ApJL, 597, L5
Henry, P. S. 1971, Natur, 231, 516
Hinshaw, G., Weiland, J. L., Hill, R. S., et al. 2009, ApJS, 180, 225
Hu, W., & Sugiyama, N. 1995, PhRvD, 51, 2599
Kaiser, N. 1984, ApJL, 284, L9
Kogut, A., Lineweaver, C., Smoot, G. F., et al. 1993, ApJ, 419, 1
Koivisto, T., & Mota, D. F. 2008, JCAP, 6, 018
Mauch, T., Murphy, T., Buttery, H. J., et al. 2003, MNRAS, 342, 1117
Milne, E. A. 1933, ZA, 6, 1
Milne, E. A. 1935, Relativity, Gravitation and World-structure (Oxford: Clarendon)
Nusser, A., & Tiwari, P. 2015, ApJ, 812, 85
Peebles, P. J. E. 1980, The Large-scale Structure of the Universe (Princeton: Princeton Univ. Press)
Penzias, A. A., & Wilson, R. W. 1965, ApJ, 142, 419
Planck Collaboration, Ade, P. A. R., Aghanim, N., et al. 2014, A&A, 571, A23
Planck Collaboration, Ade, P. A. R., Aghanim, N., et al. 2016, A&A, 594, A16
Ralston, J. P., & Jain, P. 2004, IJMPD, 13, 1857
Rigby, E. E., Best, P. N., Brookes, M. H., et al. 2011, MNRAS, 416, 1900
Řípa, J., & Shafieloo, A. 2017, ApJ, 851, 15
Řípa, J., & Shafieloo, A. 2019, MNRAS, 486, 3027
Rubart, M., & Schwarz, D. J. 2013, A&A, 555, A117
Samal, P. K., Saha, R., Jain, P., & Ralston, J. P. 2008, MNRAS, 385, 1718
Schwarz, D. J., Starkman, G. D., Huterer, D., & Copi, C. J. 2004, PhRvL, 93, 221301
Singal, A. K. 2011, ApJL, 742, L23
Smoot, G. F., Gorenstein, M. V., & Muller, R. A. 1977, PhRvL, 39, 898
Starck, J.-L., Fadili, M. J., & Rassat, A. 2013, A&A, 550, A15
Starck, J.-L., Murtagh, F., & Fadili, J. 2015, Sparse Image and Signal Processing: Wavelets and Related Geometric Multiscale Analysis (2nd ed.; Cambridge: Cambridge Univ. Press),
Tiwari, P., & Jain, P. 2015, MNRAS, 447, 2658
Tiwari, P., & Jain, P. 2019, A&A, 622, A113
Tiwari, P., Kothari, R., Naskar, A., Nadkarni-Ghosh, S., & Jain, P. 2015, APh, 61, 1
Tiwari, P., & Nusser, A. 2016, JCAP, 2016, 062
Waddington, I., Dunlop, J. S., Peacock, J. A., & Windhorst, R. A. 2001, MNRAS, 328, 882
Waddington, I., Windhorst, R. A., Dunlop, J. S., Koo, D. C., & Peacock, J. A. 2000, MNRAS, 317, 801
White, M., Scott, D., & Silk, J. 1994, ARA&A, 32, 319
Wilman, R. J., Miller, L., Jarvis, M. J., et al. 2008, MNRAS, 388, 1335